Supplementary Information (SI) for Materials Chemistry Frontiers.
This journal is © the Partner Organisations 2024

Supporting information

Regulated Dual Defects of Ligand Defects and Lattice Defects in UIO-66 for Ultra trace Simultaneous Detection and Removal of Heavy Metal Ions

Dahui An[a], Shan Jin[a], Junhua Zheng[a], Mubai Liao[a], Long Chen[a,]*

[a]School of Chemistry and Chemical Engineering/State Key Laboratory Incubation Base for Green Processing of Chemical Engineering, Shihezi University, Shihezi, 832003, China

E-mail addresses: arnoan@qq.com (D.H. An)

* Corresponding author.

E-mail addresses: chenlong2012@sinano.ac.cn (L. Chen)

Table of Contents

Section S1. Experimental Procedures 3

1.1 Materials

1.2 Material characterization

1.3 Inkjet printing

1.4 HMIs detection

1.5 HMIs adsorption

Section S2. Supplementary Characterizations and Electrochemical Results.....7

Figure S1. HRTEM and Fast Fourier Transform of D-D-UIO-66

Figure S2. Full XPS spectra of UIO-66, D-UIO-66 and D-D-UIO-66

Figure S3. Simultaneous detection of D-UIO-66 for Cd(II), Pb(II) Cu(II) and Hg(II).

Figure S4. Simultaneous detection of D-D-UIO-66 for Cd(II), Pb(II) Cu(II) and Hg(II).

Figure S5. CV curves of D-D-UIO-66 /GCE in the solution containing 5.0 mM $[Fe(CN)_6]^{3-/4-}$ and 0.1 M KCl and the linear relationship between the anodic peak currents and the square root of scan.

Figure S6. CV curves of D-UIO-66 /GCE in the solution containing 5.0 mM $[Fe(CN)_6]^{3-/4-}$ and 0.1 M KCl and the linear relationship between the anodic peak currents and the square root of scan.

Figure S7. The reproducibility of D-D-UIO-66

Figure S8. The stability of D-D-UIO-66

Figure S9. DPASV curves in Shuxiang Lake in Shihezi, China for the Cd(II), Pb(II)

Cu(II) and Hg(II).

Figure S10. DPASV curves in Yangtze River Main Stream (Anhui Section) in Tongling, China for the Cd(II), Pb(II) Cu(II) and Hg(II)

Figure S11. The comparison of Cd(II), Pb(II) Cu(II) and Hg(II) sensitivity in different types of water

Figure S12. O 1s XPS Spectra of D-D-UIO-66 before and after adsorption.

Figure S13 FT-IR spectra of UiO-66 ,D-UiO-66 and D-D-UIO-66.

Table S1 Compared with other materials Pb(II) detection performance

Table S2 Comparison of individual and simultaneous detection

Table S3. Langmuir and Freundlich adsorption parameters for Pb(II) on the four adsorbents at 298 K.

Table S4. Estimates of parameter values for the adsorption of Pb(II) on adsorbents at 298 K according to the pseudo-first-order and pseudo-second-order models.

Table S5 Comparison of LOD and theoretical adsorption capacity for Pb(II) with other bifunctional materials.

Table S6 Comparison of theoretical adsorption capacity for Pb(II) with other monofunctional materials.

Section S3. References 23

1. Experimental

1.1 Materials

All chemicals were analytically pure and were used as purchased, without any further purifications. Zirconyl Chloride Octahydrate, 98% was purchased from Shanghai Adamas Reagent Co., Ltd. Absolute ethanol, Cerium nitrate hexahydrate 99.5%, Trifluoroacetic acid AR, p-Phthalic acid 99% were purchased from Shanghai Macklin Biochemical Technology Co., Ltd. Deionized water was used throughout the electrochemical measurements and materials preparation.

1.2 Material characterization

The synthesized D-D-UIO-66 materials were characterized by the powder X-ray diffraction (XRD; Rigaku XRD-6100, Japan); scanning electron microscopy (SEM, Hitachi SU8010, Japan) with energy dispersive X-ray spectroscopy (EDX) and transmission electron microscopy (TEM; FEI Talos F200X G2, USA); X-ray photoelectron spectroscopy (XPS; Thermo Scientific K-Alpha, USA) was conducted using monochromatic Al Kα X-ray source; The specific surface areas were obtained from N_2 adsorption desorption isotherms at 77 K with BET surface area analyzer (BET; Micromeritics, ASAP 2460, GA, USA); Thermogravimetric analysis (TG) measurements were made with a DSC/DTA-TG unit (Rigaku TG/DTA8122, Japan) under N_2 atmosphere from 30 ℃ to 800 ℃ at heating rate of 10 ℃ min^{-1}; The concentration of HMIs was determined by a ContrA 700 (Analytik Jena, Germany) Inductively Coupled Plasma-Atomic Emission Spectrometry (ICP-AES).

1.3Inkjet printing

The ink was filtrated through a filter with a pore size of 0.45 μm before printing. Picolitre drops of the ink were ejected from a dope-on-demand inkjet system RD-PMF100 (MicroFab Technologies) onto the glassy carbon electrode (GCE). Printing was performed at a voltage pulse of 27 V with a droplet velocity of 1.24 m s^{-1}

1.4 HMIs detection

All electrochemical experiments were performed on an electrochemical workstation (CHI 760E, CH Instruments Inc., Shanghai, China) with a conventional three-electrode system, where the bare or D-D-UIO-66/GCE modified electrode, Ag/AgCl and platinum wire electrode served as the working, reference, and auxiliary electrodes, respectively. The differential pulse anodic stripping voltammetry (DPASV) measurement was utilized for the observation of electrochemical detection behavior toward Pb(II), Cd(II), Cu(II), and Hg(II) under optimized experimental conditions. The actual water is first filtered to remove insoluble impurities, then diluted with a 0.1 M HAc−NaAc buffer solution to form a real water sample with a volume ratio of 1:9.

1.5 HMIs adsorption

Adsorption isotherms. During an isotherm adsorption experiments, 20 mg adsorbents were dispersed in 20 mL Pb(II) aqueous solution with initial concentrations ranged from 100 to 1000 mg L^{-1}. The adsorption process performed in a shaker at 200 rpm for 700 minutes at 25 ℃. The adsorption capacity of Pb(II) on four adsorbents was calculated using Eq. (1):

$$Q_e = \frac{V(C_0 - C_e)}{m} \quad (1)$$

Where Q_e is the equilibrium adsorption capacity (mg L^{-1}), C_0 and C_e are the initial and equilibrium concentration of Pb(II) (mg L^{-1}), respectively, m is the mass of adsorbents (g), V is the

volume of Pb(II) solution (L). The isotherm adsorption dates were analyzed using Langmuir Eq. (2) and the Freundlich Eq. (3) isotherm model at 25 °C

$$Q_e = \frac{K_L Q_m C_e}{1 + K_L C_e} \quad (2)$$

$$Q_e = K_F C_e^{1/n} \quad (3)$$

Where C_e (mg g^{-1}) is the equilibrium concentration of the Pb(II) solution, Q_e (mg g^{-1}) is the equilibrium adsorption capacity of the adsorbent, Q_m (mg g^{-1}) is the theoretical maximum adsorption capacity, K_L (L mg^{-1}) represents Langmuir constant, K_F ($mg^{-1/n}$ $L^{-1/n}$ g^{-1}) and n represents Freundlich constant.

Adsorption kinetics. Adsorption kinetics was conducted by adding 100 mg of the four adsorbents into a 100 mL Pb(II) solution with initial concentrations 1000 mg L^{-1} at 25 °C. The kinetic dates were examined by the pseudo-first-order Eq. (4) and pseudo-second-order model Eq. (5):

$$ln\,(Q_e - Q_t) = lnQ_m - k_1 t \quad (4)$$

$$\frac{t}{Q_t} = \frac{1}{k_2 Q_m^2} + \frac{t}{Q_m} \quad (5)$$

Where Q_t is the adsorption capacity of the adsorbent at time t and Q_m (mg g^{-1}) and at equilibrium, respectively, k_1 (min^{-1}) and k_2 (g mg^{-1} min^{-1}) are the corresponding rate constants.

2. Results and discussion

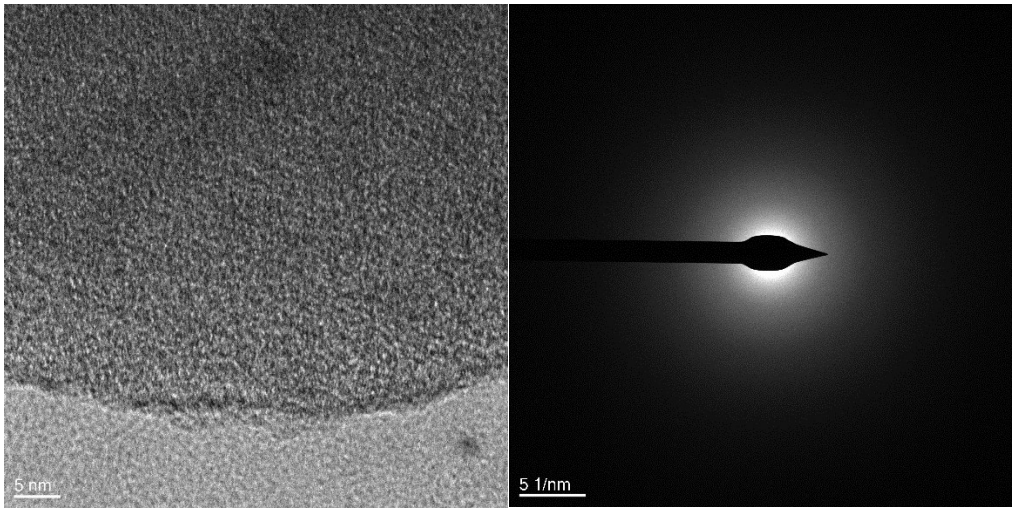

Figure S1 HRTEM and Fast Fourier Transform of D-D-UIO-66

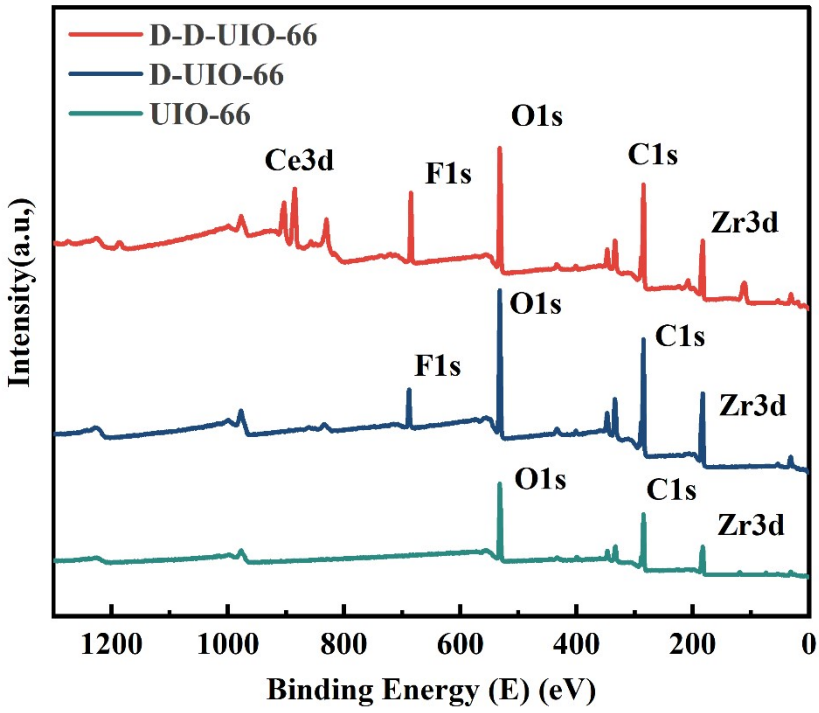

Figure S2 Full XPS spectra of UIO-66, D-UIO-66 and D-D-UIO-66

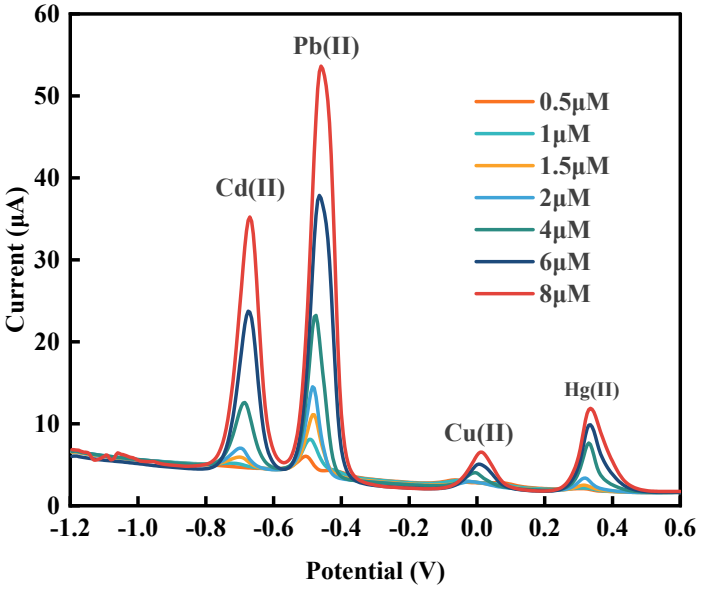
Pb(II)
Cd(II)
Cu(II)
Hg(II)
0.5μM
1μM
1.5μM
2μM
4μM
6μM
8μM
Current (μA)
Potential (V)

122

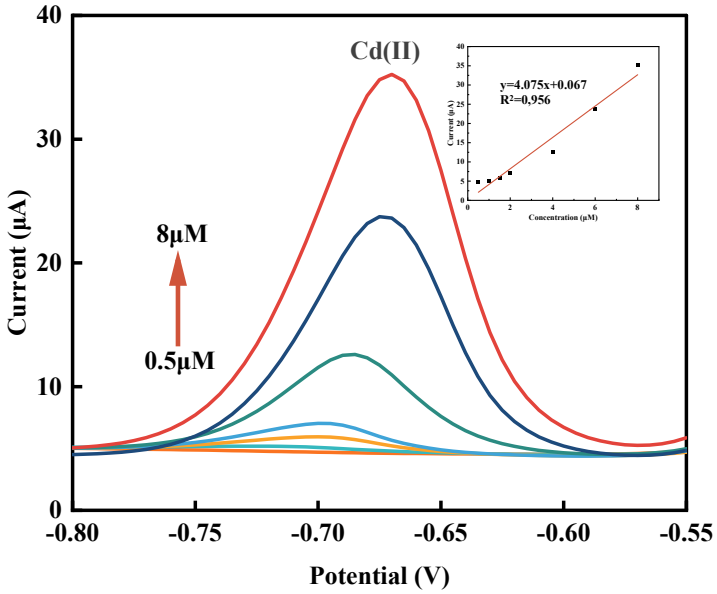
Cd(II)
y=4.075x+0.067
R²=0.956
Concentration (μM)
8μM
0.5μM
Current (μA)
Potential (V)

123

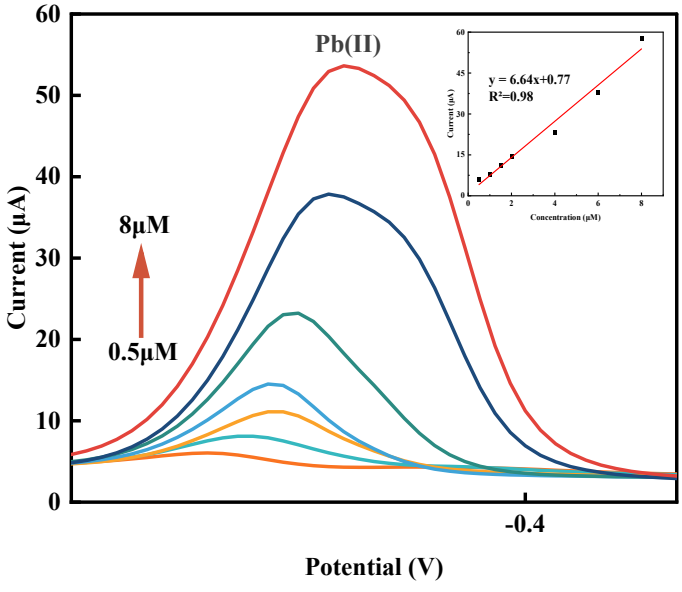
Pb(II)
y = 6.64x+0.77
R²=0.98
Concentration (μM)
8μM
0.5μM
Current (μA)
Potential (V)

124

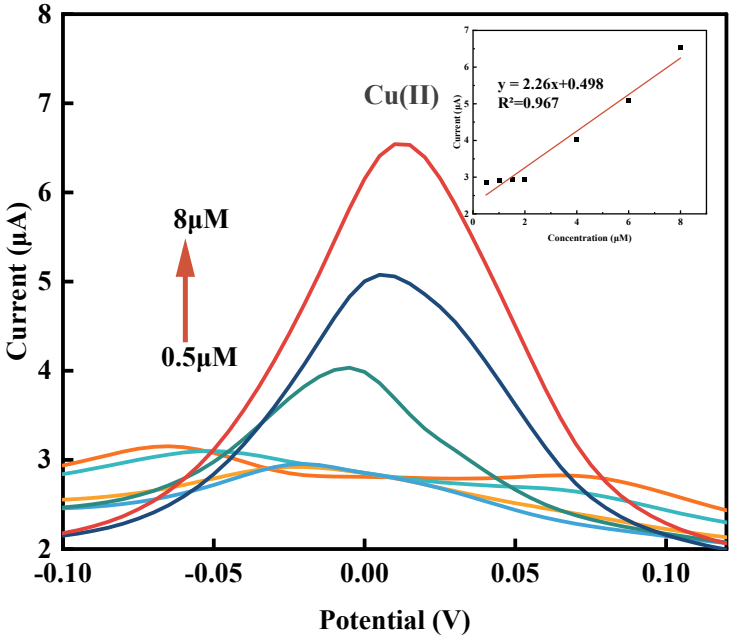

125

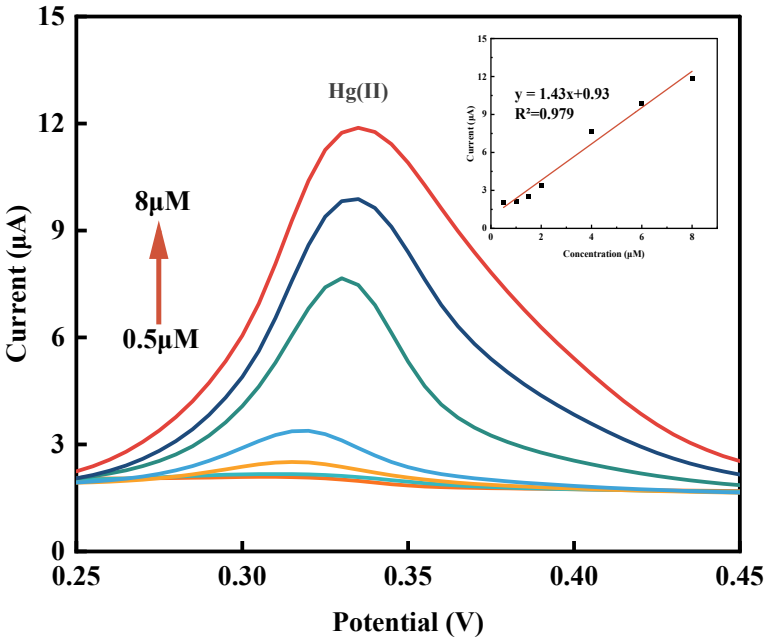

126

127 Figure S3 Simultaneous detection of D-UIO-66 for Cd(II), Pb(II) Cu(II) and Hg(II).

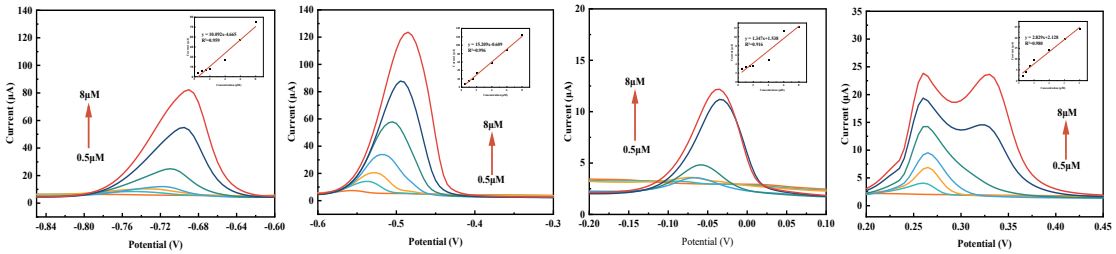

128

129 Figure S4 Simultaneous detection of D-D-UIO-66 for Cd(II), Pb(II) Cu(II) and Hg(II).

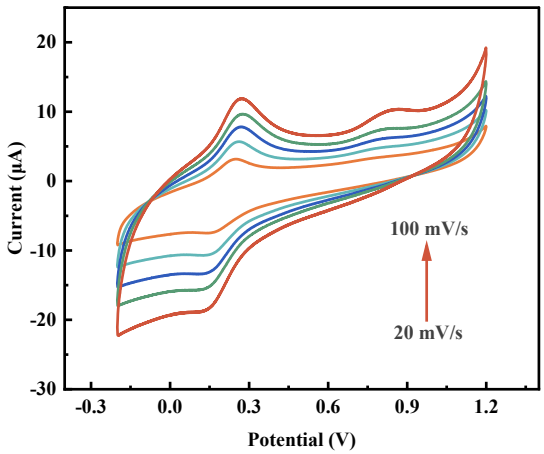

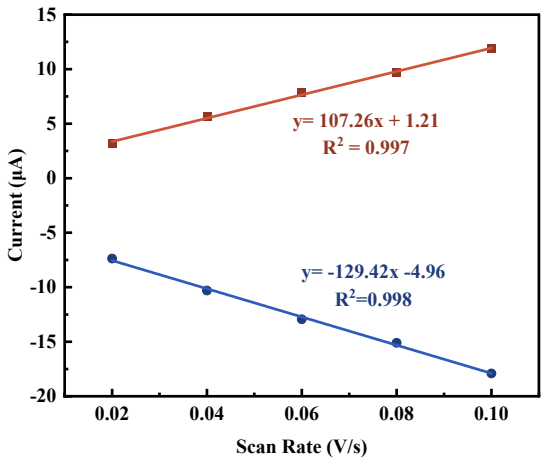

Figure S5 CV curves of D-D-UIO-66 /GCE in the solution containing 5.0 mM $[Fe(CN)_6]^{3-/4-}$ and 0.1 M KCl and the linear relationship between the anodic peak currents and the square root of scan.

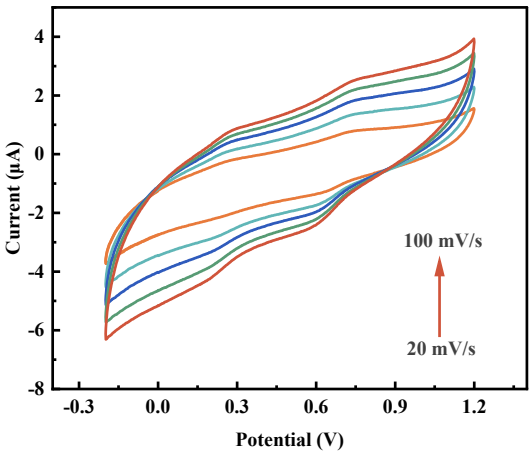

136

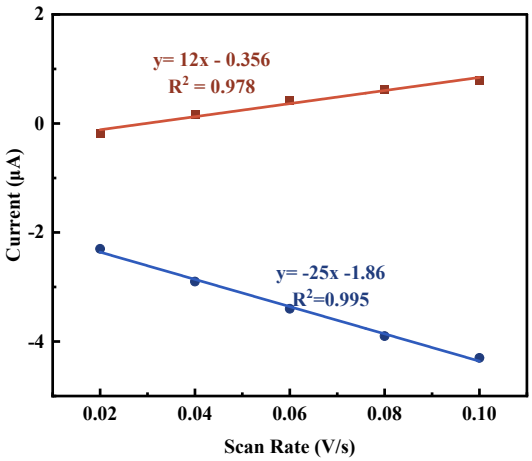

137

138 Figure S6 CV curves of D-UIO-66 /GCE in the solution containing 5.0 mM

139 $[Fe(CN)_6]^{3-/4-}$ and 0.1 M KCl and the linear relationship between the anodic peak

140 currents and the square root of scan.

141

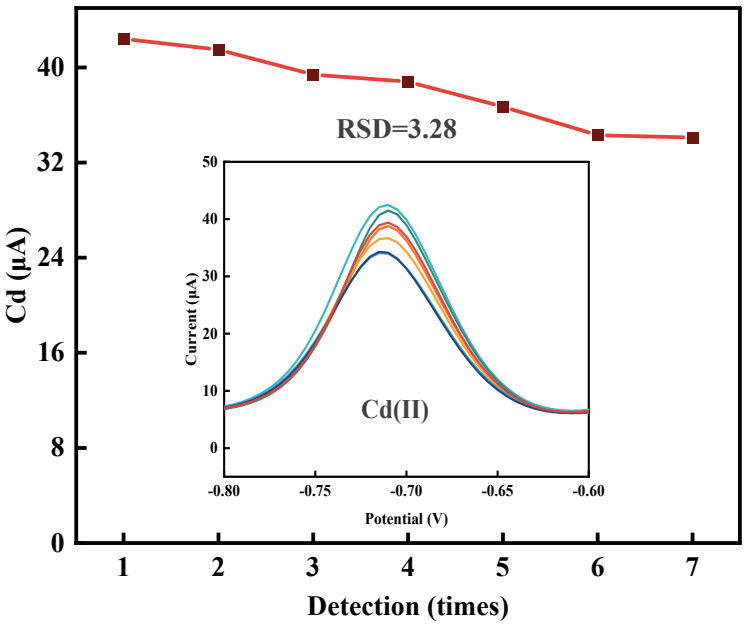
RSD=3.28
Cd (μA)
Detection (times)
Current (μA)
Potential (V)
Cd(II)

142

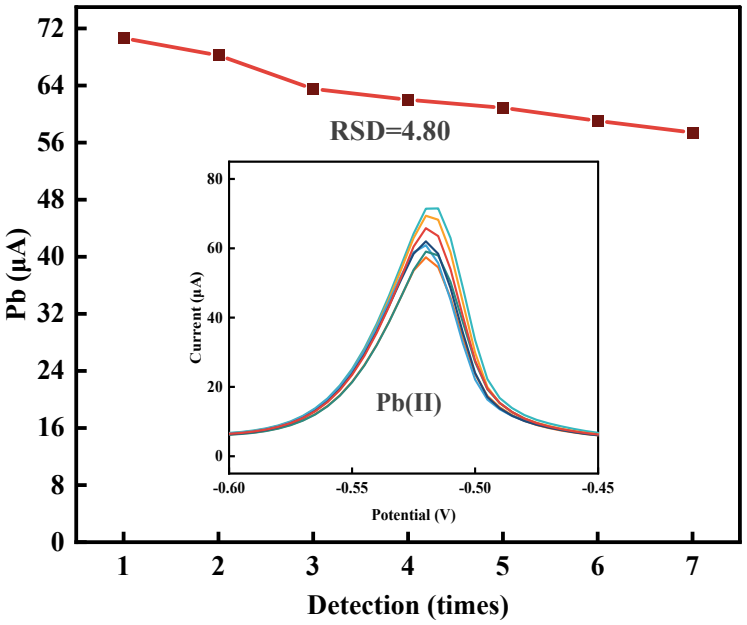
RSD=4.80
Pb (μA)
Detection (times)
Current (μA)
Potential (V)
Pb(II)

143

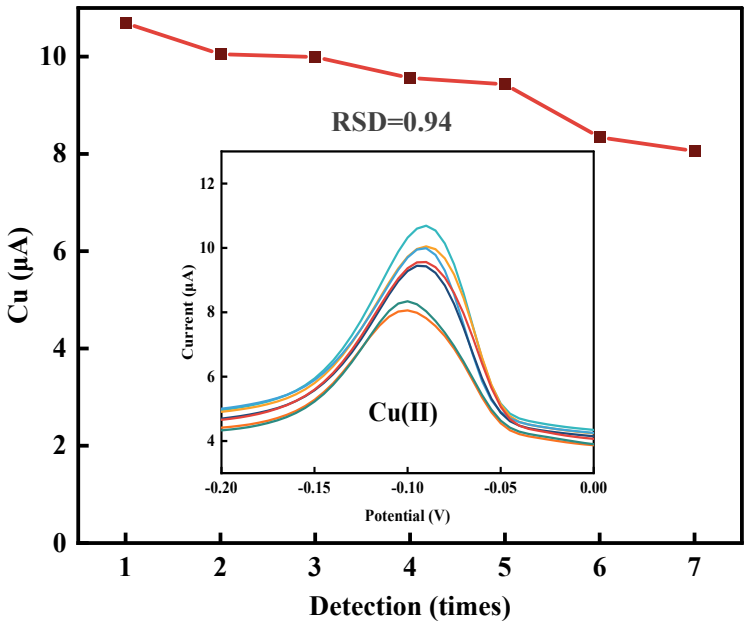

144

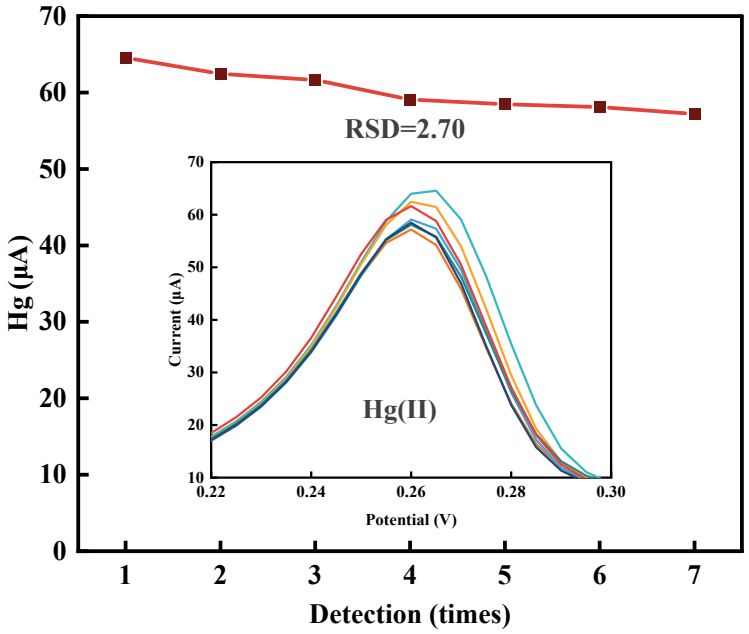

145

146 Figure S7 The reproducibility of D-D-UIO-66.

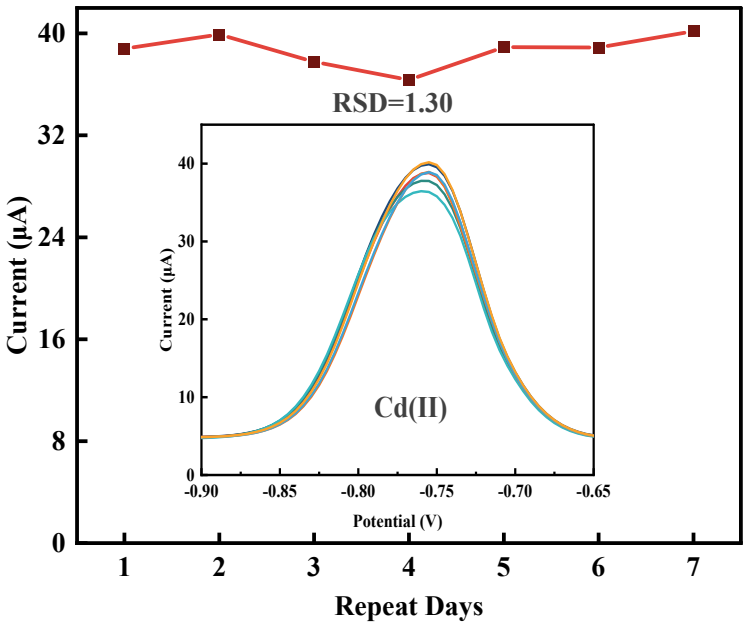
RSD=1.30
Cd(II)
Current (μA)
Potential (V)
Repeat Days

147

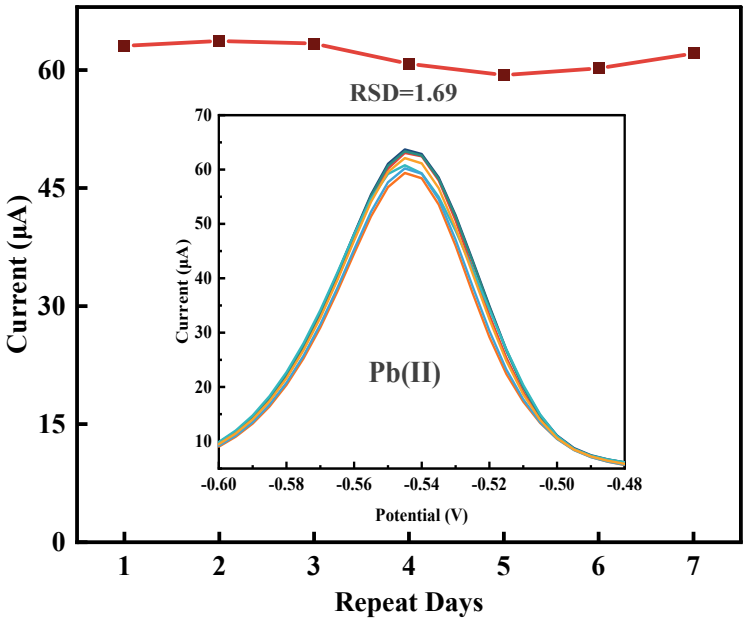
RSD=1.69
Pb(II)
Current (μA)
Potential (V)
Repeat Days

148

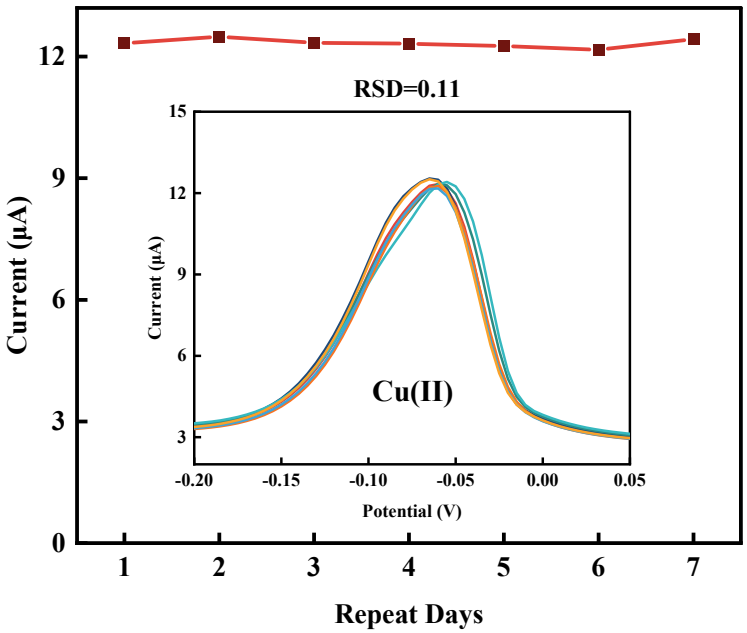

149

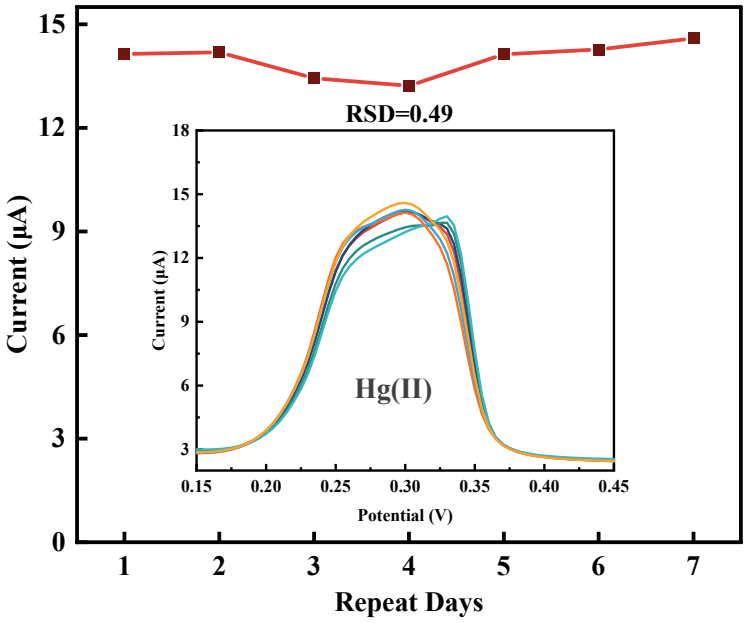

150

151 Figure S8 The stability of D-D-UIO-66.

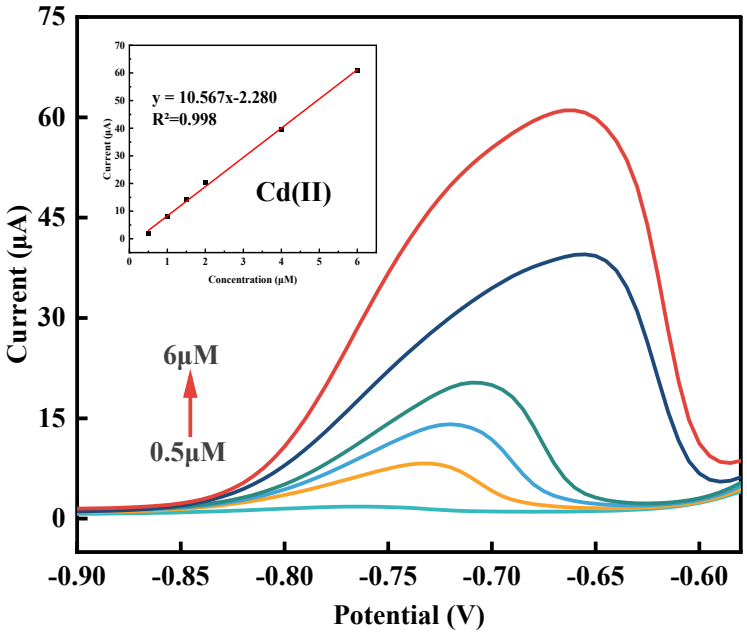
y = 10.567x-2.280
R²=0.998
Cd(II)
Concentration (μM)
Current (μA)
6μM
0.5μM
Current (μA)
Potential (V)

152

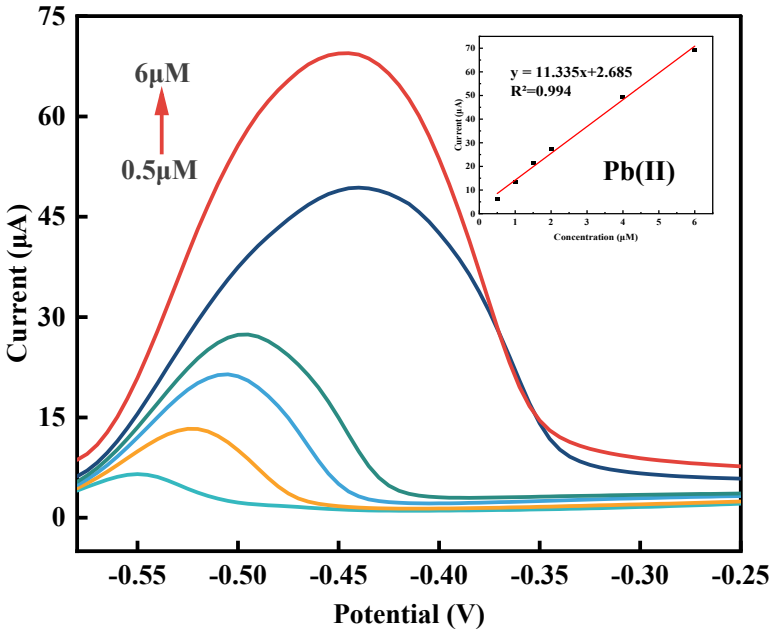
6μM
0.5μM
y = 11.335x+2.685
R²=0.994
Pb(II)
Concentration (μM)
Current (μA)
Potential (V)

153

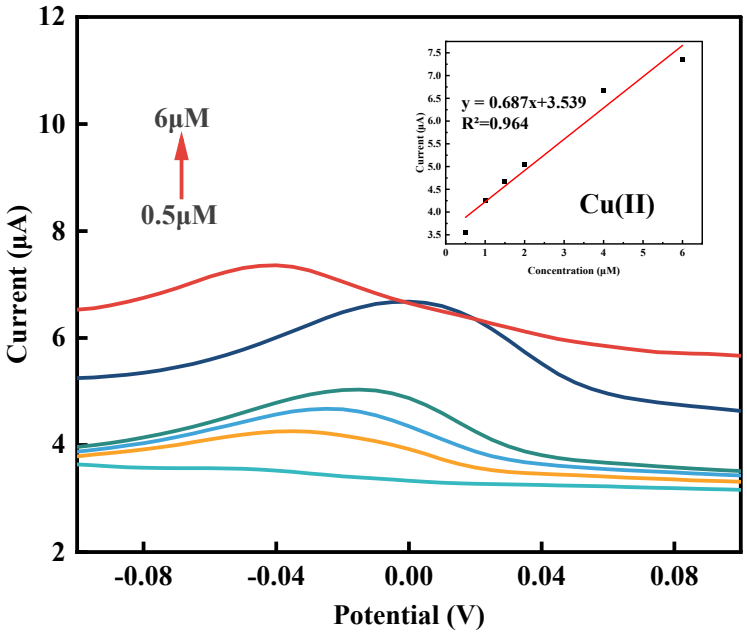

154

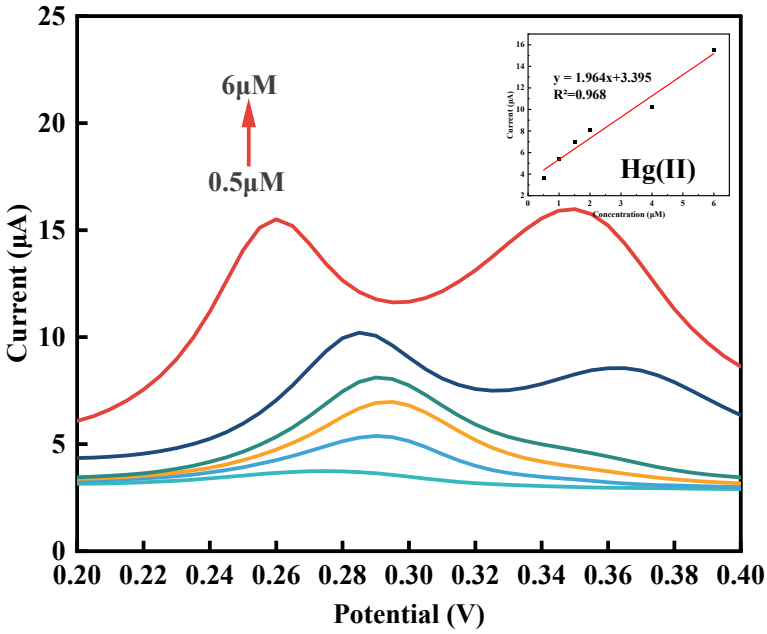

155

156 Figure S9 the DPASV curves in Shuxiang Lake in Shihezi, China for the Cd(II),

157 Pb(II) Cu(II) and Hg(II).

158

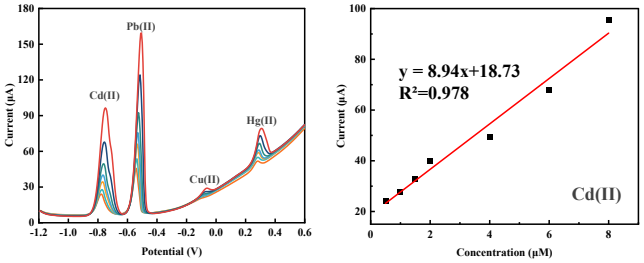

159

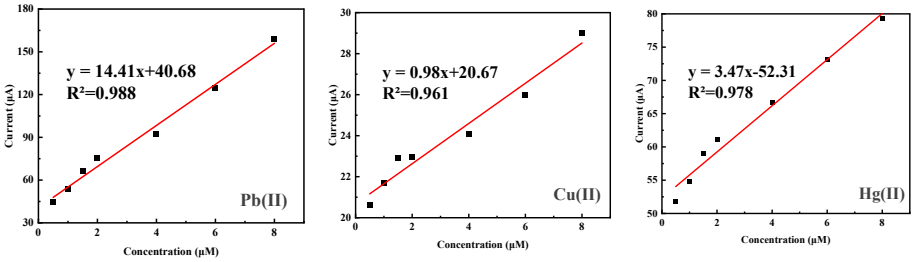

160 Figure S10 DPASV curves in Yangtze River Main Stream (Anhui Section)

161 (Tongling, China) for the Cd(II), Pb(II) Cu(II) and Hg(II)

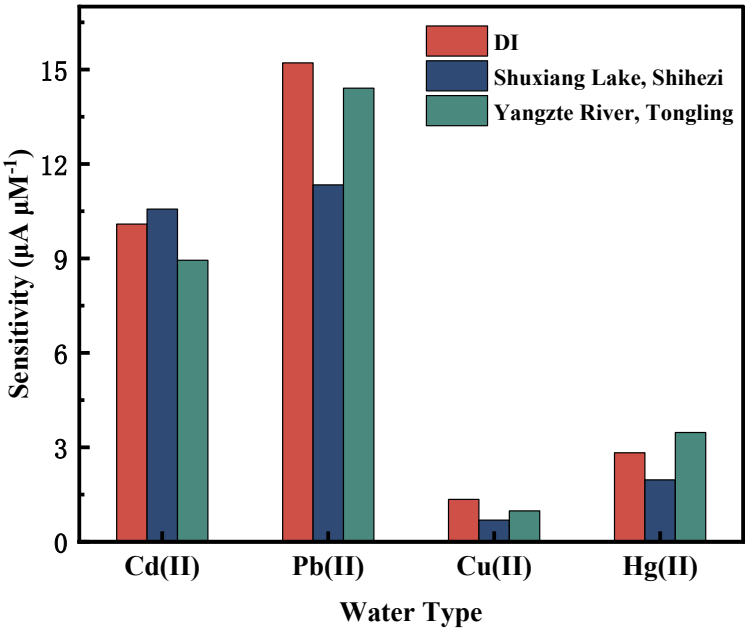

162

163 Figure S11 The comparison of Cd(II), Pb(II) Cu(II) and Hg(II) sensitivity in

164 different types of water

165

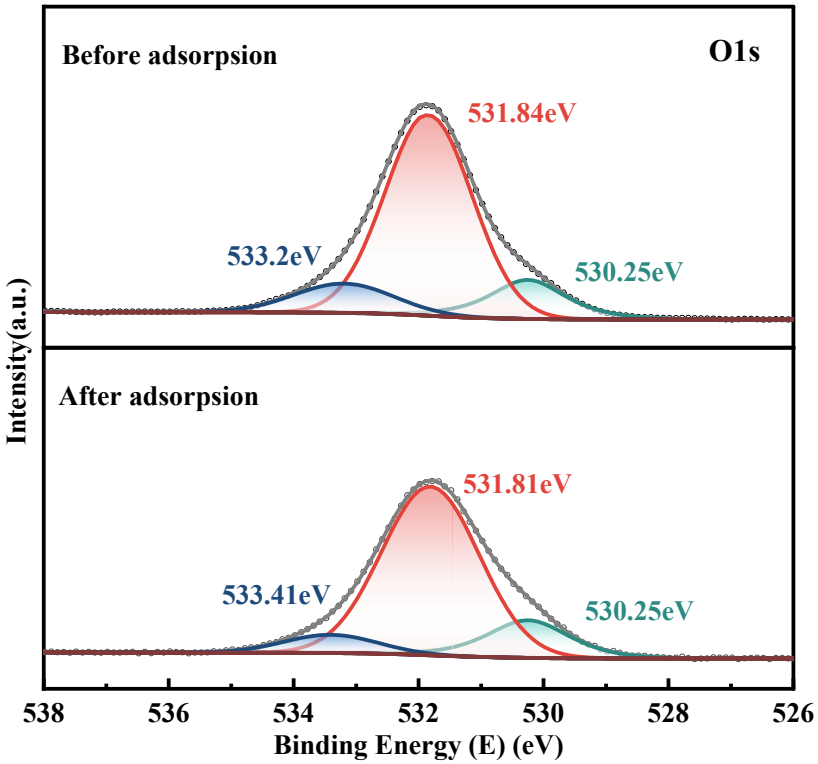

166

167 Figure S12 O 1s XPS Spectra of D-D-UIO-66 before and after adsorption.

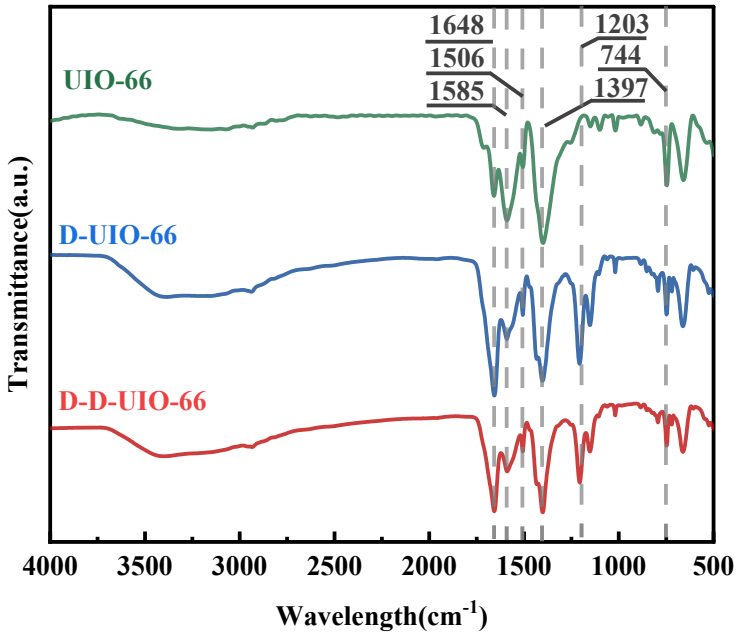

168

169 Figure S13 FT-IR spectra of UiO-66 ,D-UiO-66 and D-D-UIO-66.

170

171

Table S1 Compared with other materials Pb(II) detection performance

Electrodes	Method	Sensitivity ($\mu A\ \mu M^{-1}$)	Detection limit (nM)	References
Bi/Bi2O3@C	DPASV	3.35	6.3	1
BCN-Nafion/GCE	SWASV	0.509	0.9	2
Fe3O4@MPC-2/GCE	DPASV	22.3	12.1	3
Fe@YAU-101/GCE	DPASV	0.596	33.3	4
e-CuFe-PBA/GCE	DPASV	24.915	28.7	5
α-MoO	SWASV	0.033	9.72	6
g–C3N4–P(Ani-Py)-PAAM	DPASV	1.2906	14.84	7
Cu-Co3O4 MCNS	DPASV	20.59	20.9	8
ALA/pDA/rGO	DPASV	15.41	13.774	9
D-D-UIO-66 (This work)	DPASV	20.204	5.965	

Table S2 Comparison of individual and simultaneous detection

	HMIs	Sensitivity ($\mu A\ \mu M^{-1}$)	R^2
Simultaneous detection	Cd (II)	10.092	0.959
	Pb (II)	15.209	0.996
	Hg (II)	1.347	0.916
	Cu (II)	2.829	0.980
Individual detection	Cd (II)	12.838	0.993
	Pb (II)	20.204	0.989
	Hg (II)	1.668	0.969

	Cu (II)	2.387	0.983

176

177 Table S3. Langmuir and Freundlich adsorption parameters for Pb(II) on the four adsorbents at 298

178 K.

Adsorbents	Langmuir isotherm parameters			Freundlich isotherm parameters	
	Q_m (mg g^{-1})	K_L (*10^{-3}) (L mg^{-1})	R^2	K_F ($mg^{1-(1/n)} L^{1/n} g$)	R^2
D-UIO-66	416.85	0.0001	0.9864	0.301	0.9440
D-D-UIO-66	667.04	0.0156	0.9968	0.473	0.9848

179

180 Table S4. Estimates of parameter values for the adsorption of Pb(II) on adsorbents at 298 K

181 according to the pseudo-first-order and pseudo-second-order models.

Adsorbents	pseudo-first-order			pseudo-second-order		
	Q_e (mg g^{-1})	K_1 (min^{-1})	R^2	Q_m (mg g^{-1})	K_2 (*10^{-4}) (g mg^{-1} min^{-1})	R^2
D-UIO-66	349.94	0.126	0.982	364.823	6.798	0.991
D-D-UIO-66	385.92	0.128	0.969	402.40	6.184	0.973

182

183 Table S5 Comparison of LOD and theoretical adsorption capacity for Pb(II) with other

184 bifunctional materials

Absorbent	Q_m (mg g^{-1})	Detection limit (nM)	References
BUC-77	425	33.36	10
IIMB	124.07	4.58	11
FSH-6	265.9	0.289	12

NBW	211.6	0.627	13
CDs	183	-	14
D-D-UIO-66	667.04	5.965	This work

185

186 Table S6 Comparison of theoretical adsorption capacity for Pb(II) with other monofunctional

187 materials

Absorbent	Q_m (mg g^{-1})	References
SALDETA@CPTMS@Fe_3O_4	415.5	15
Fe-LAA	508.2	16
A/M-CDMOF	414.2	17
MOF-DFSA	349.09	18
D-D-UIO-66	667.04	This work

188

189

References

1 Wang, C.; Niu, Q.; Liu, D.; Dong, X.; You, T. Electrochemical Sensor Based on Bi/Bi_2O_3 Doped Porous Carbon Composite Derived from Bi-MOFs for Pb^{2+} Sensitive Detection. *Talanta* **2023**, **258**, 124281.

2 Huang, R.; Lv, J.; Chen, J.; Zhu, Y.; Zhu, J.; Wågberg, T.; Hu, G. Three-Dimensional Porous High Boron-Nitrogen-Doped Carbon for the Ultrasensitive Electrochemical Detection of Trace Heavy Metals in Food Samples. *J. Hazard. Mater.* **2023**, **442**, 130020.

3 Liu, Y.; Wu, S.; Xiong, W.; Li, H. Interface Co-Assembly Synthesis of Magnetic Fe_3O_4@Mesoporous Carbon for Efficient Electrochemical Detection of Hg^{2+} and Pb^{2+}. *Adv. Mater. Interfaces* **2023**, **105**, 2201631.

4 Liang, Q.; Xiao, W.; Zhang, C.; Zhu, D.; Wang, S.-L.; Tian, S.-Y.; Long, T.; Yue, E.-L.; Wang, J.-J.; Hou, X.-Y. MOFs-Based Fe@YAU-101/GCE Electrochemical Sensor Platform for Highly Selective Detecting Trace Multiplex Heavy Metal Ions. *Talanta* **2023**, **259**, 124491.

5 Jin, S.; Pang, J.; Ma, F.; Cheng, Y.; Shen, Y.; Xiao, Z.; Chen, L. Regulating Valence States of CuFe-PBA for the Simultaneous Electrochemical Detection of Cd^{2+}, Pb^{2+} and Hg^{2+} in Food Application. *Talanta* **2024**, **273**, 125848.

6 Li, P.-H.; Song, Z.-Y.; Yang, M.; Chen, S.-H.; Xiao, X.-Y.; Duan, W.-C.; Li, L.-N.; Huang, X.-J. Electrons in Oxygen Vacancies and Oxygen Atoms Activated by Ce^{3+}/Ce^{4+} Promote High-Sensitive Electrochemical Detection of Pb^{2+} Over Ce-Doped α-MoO_3 Catalysts. *Anal. Chem.* **2020**, **9224**, 16089-16096.

7 Xiao, L.; Zhao, Y.; Chang, G.; Yan, H.; Zou, R.; Zhang, X.; Wang, S.; He, H. A 3D Phytic Acid Cross-Linked High-Porous Conductive Hydrogel Integrating g-C_3N_4 for Electrochemical

Multiplex Sensing of Heavy Metal Ions. *Anal. Chim. Acta* **2023**, **1269**, 341341.

8 Pang, J.; Sun, K.; Jin, S.; Hou, J.; Wang, G.; Sun, K.; Zheng, Y.; Zhang, Y.; Chen, L. Oxygen Vacancies Enriched Multi-Channel-Like Metal-Doped Co_3O_4 Nanosheets by Lewis Acid Etching for Detection of Small Biological Molecules in Apple Juice and Wine. *Chem. Eng. J.* **2023**, **454**, 140085.

9 Patel, M.; Bisht, N.; Prabhakar, P.; Sen, R. K.; Kumar, P.; Dwivedi, N.; Ashiq, M.; Mondal, D. P.; Srivastava, A. K.; Dhand, C. Ternary Nanocomposite-Based Smart Sensor: Reduced Graphene Oxide/Polydopamine/Alanine Nanocomposite for Simultaneous Electrochemical Detection of Cd^{2+}, Pb^{2+}, Fe^{2+}, and Cu^{2+} Ions. *Environ. Res.* **2023**, **221**, 115317.

10 Song, X.; Fu, H.; Wang, P.; Li, H. Y.; Zhang, Y. Q.; Wang, C. C. The Selectively Fluorescent Sensing Detection and Adsorptive Removal of Pb^{2+} with a Stable [δ-Mo_8O_{26}]-Based Hybrid. *J. Colloid Interface Sci.* **2018**, **532**, 598-604.

11 Wu, P.; He, Y.; Lu, S.; Wang, S.; Yi, J.; He, Y.; Zhang, J.; Xiang, S.; Ding, P.; Kai, T.; Pan, H. A Regenerable Ion-Imprinted Magnetic Biocomposite for Selective Adsorption and Detection of Pb^{2+} in Aqueous Solution. *J. Hazard. Mater.* **2021**, **408**, 124410.

12 Zhang, Z.; Huang, Z.; Qin, D.; Liu, D.; Guo, X.; Lin, H. Fluorescent Starch-Based Hydrogel with Cellulose Nanofibrils and Carbon Dots for Simultaneous Adsorption and Detection of Pb^{2+}. *Carbohydr. Polym.* **2024**, **323**, 121427.

13 Qi, X.; Chen, Y.; Liu, M.; Zhang, X.; Zuo, Y.; Ma, Q.; Xie, X.; Guo, X.; Wu, Y. Green and Cost-Effective: Bifunctional Wood for Efficient Adsorption and Sensitive Detection of Pb^{2+}. *Ind. Crops Prod.* **2024**, **210**, 118162.

14 Jing, L.; Ding, Q.; Li, X.; Lou, J.; Liu, Z.; Jiang, Y.; Han, W.; Cheng, Z. Bifunctional Collagen

234 Fiber/Carbon Quantum Dot Fluorescent Adsorbent for Efficient Adsorption and Detection of
235 Pb^{2+}. *Sci. Total Environ.* **2023**, **871**, 161989.
236 15 Solanki, K.; Sharma, S.; Rana, P.; Kaushik, B.; Yadav, S.; Dixit, R.; Birdar, A. V.; Gupta, A.;
237 Sharma, R. K. A Structurally Engineered Flower Shaped Magnetic Hierarchical Sorbent for
238 Rapid and Selective Uptake of Pb^{2+} Ions from Water Samples. *Mater. Chem. Front.* **2023**, **7**
239 (19), 4482-4496.
240 16 Chowdhury, S. S.; Roy, D.; De, S. Facile Green Synthesis of Novel Iron Aspartate (Fe-LAA)
241 MOF for Adsorptive Mitigation of Lead (Pb) from Water. *J. Clean. Prod.* **2023**, **426**, 139146.
242 17 Jia, J.; Zhu, J.; Guo, L.; Yu, J.; Li, J.; Li, F. Synthesis and Characterization of a β-Cyclodextrin-
243 MOF-Based Porous Hydrogel for Efficient Adsorption of Au^{3+}, Ag^{+}, and Pb^{2+} Ions. *Sep. Purif.*
244 *Technol.* **2024**, **348**, 127664.
245 18 Wang, H.; Wang, S.; Wang, S.; Fu, L.; Zhang, L. The One-Step Synthesis of a Novel Metal–
246 Organic Framework for Efficient and Selective Removal of Cr (VI) and Pb (II) from
247 Wastewater: Kinetics, Thermodynamics, and Adsorption Mechanisms. *J. Colloid Interface Sci.*
248 **2023**, **640**, 230-245.
249